PCCP

ARTICLE TYPE

Cite this: DOI: 00.0000/xxxxxxxxxx

Received Date
Accepted Date

DOI: 00.0000/xxxxxxxxxx

Refractive index dispersion measurement in the short-wave infrared range using synthetic phase microscopy

Melisa Nyakuchena,[a] Cory Juntunen,[a] Peter Shea,[a] and Yongjin Sung*[a]

Refractive index is an optical property explored in the light scattering measurement of micro- and nano-particles as well as in label-free imaging of cells and tissues. Because the refractive index value is a major input to the characterization and quantification of the analyzed specimens, various methods have been developed targeting at different sample types. In this paper, we demonstrate a technique for the refractive index measurement of homogeneous microspheres and liquids in the short-wave infrared (SWIR) range. We use synthetic phase microscopy (SPM), which records a scattering-corrected projection of the 3D refractive index distribution, in combination with a least-squares fitting to a theoretical model of a sphere. Using the method, we determine the refractive index dispersion of two polymer microspheres (polymethyl methacrylate and polystyrene), two glass microspheres (silica and soda lime), and three microscopy mounting media (glycerol, FluorSave, and Eukitt) in the SWIR range of 1100–1650 nm.

1 Introduction

Hyperspectral imaging in the short-wave infrared (SWIR) range is being actively explored owing to its large penetration depth and sensitivity to chemical fingerprints[1,2]. Refractive index is a key optical property in the light scattering measurement of powders, microplastics, synthesized nanoparticles, etc.[3]. Refractive index also serves as an image contrast in label-free imaging of cells and tissues[4] and determines the amount of scattering from tissues[5]. For the refractive index of liquids, Abbe refractometry is the gold standard method, which uses the total internal reflection of the incident light at the interface of a prism and the interrogated medium. Using Abbe refractometry in combination with band-pass filters, the refractive index can be determined over a broad wavelength range, for example, Kedenburg et al. (2012)[6]. Abbe refractometry is very accurate, but it is cumbersome, although not impossible, to measure the refractive index of solidifying media such as microscopy mounting media, as the hardened media will have to be scraped off the surface after each measurement. For a homogeneous material with a planar interface, ellipsometry can provide accurate refractive index values over a broad wavelength range, for example, Tsuda et al. (2018)[7]. For a microsphere, the scattering analysis using the Mie solution has been used to determine the refractive index, for example, McGrory et al. (2020)[8] and Muller et al. (2018)[9]. The refractive index dispersion has also been determined from an interferometry-based phase measurement technique in combination with a wavelength-scanning light source[10,11]. Here we use a phase imaging technique called synthetic phase microscopy (SPM)[12]. The optical field synthesis has been demonstrated to improve the resolution and suppress the noise[13,14]. SPM aims at a different goal correcting for the diffraction effect and providing a true projection image irrespective of the sample's thickness. Applying SPM to a microsphere and applying a least-squares fit to the theoretical model for a sphere, we measure the refractive index of four microspheres (two polymer and two glass microspheres) and three microscopy mounting media in the SWIR range.

Assuming the light propagates rectilinearly across a sample, the phase distribution of light after the sample can be directly related to the refractive index of the sample and that of the medium by Eq. (1)[15].

$$\Phi(x,y;\lambda) = (2\pi/\lambda)\int (n_s(x,y,z) - n_m)\,dz, \tag{1}$$

where x and y are the transverse coordinates, z is the optical axis direction, $n_s(x,y,z)$ is the 3D refractive index distribution within the sample, and n_m is the refractive index of the medium in which the sample is immersed.

Noteworthy, the assumption that the light propagates rectilinearly across a sample is not valid when including the refraction of light rays at the top and bottom surfaces of the microsphere and their diffraction at the boundary. The coherent speckle and an oblique incidence of the illumination beam can also challenge the validity of Eq. (1). To address these problems, we use SPM, which synthesizes the true projection image from a multitude of the phase images acquired for varying illumination angles[12]. Derived from the scalar wave equation, the algorithm used for SPM handles the refraction and diffraction effects. Using many pro-

---

[a] Address, 3200 N Cramer St, Milwaukee, WI, USA. E-mail: ysung4@uwm.edu

jection images, SPM also smoothes out coherent speckle noise. SPM synthesizes the projection image along the optical axis direction; thus, the problem with the oblique illumination angle can be solved.

With the projection images acquired for varying angles, digital holographic tomography (DHT), also called tomographic phase microscopy[16] or tomographic diffractive microscopy[17], can determine the 3D refractive index distribution within a heterogeneous, non-spherical specimen[18]. The technique has also been demonstrated for hyperspectral 3D refractive index imaging in the optical wavelength range[19–21]. However, the accuracy of 3D refractive index imaging using DHT is seriously compromised due to incomplete angular sampling—the problem known as the missing-cone problem[22]. The regularization using additional constraints is known to alleviate the problem[22,23]; however, the result depends on a rather subjective selection of the hyperparameters such as the number of iterations[24]. Here we use the projection images to synthesize a single phase image, in which the effect of refraction and diffraction has been corrected. Applying the method to a microsphere and using a least-squares fit, we can provide the refractive dispersion of the microsphere or the immersion liquid at higher accuracy than the existing phase measurement techniques can provide.

The phase distribution of light after a homogeneous sample immersed in a medium can be derived from Eq. (1) as follows.

$$\Phi(x,y;\lambda) = (2\pi/\lambda)\,(n_s - n_m)\,\Delta h, \tag{2}$$

where n_s and n_m are the refractive index values of the sample and the medium, respectively, and Δh is the thickness of the sample at a transverse location (x,y). For a microsphere of radius R, centered at (x_0,y_0), the thickness can be expressed as follows.

$$\Delta h = 2\sqrt{R^2 - (x-x_0)^2 - (y-y_0)^2}. \tag{3}$$

Fitting the phase distribution in the true projection image to Eq. (2), the theoretical equation for a sphere, we can determine n_m, when n_s is known, and vice versa. Other parameters such as the radius R and the center coordinates (x_0,y_0) of the microsphere are also determined in the fitting.

2 Methods

2.1 Synthetic phase microscopy (SPM)

We have built a SWIR digital holographic tomography (DHT) system upon an off-axis Mach-Zehnder interferometer. Fig. 1(a) shows a schematic diagram of the setup. For the light source, we use a supercontinuum laser (NKT Photonics, WL SC400-4) coupled with a tunable filter (NKT Photonics, SWIR HP8), which provides a quasi-monochromatic light with the bandwidth (FWHM) smaller than 5 nm in the range of 1000–2300 nm. After the tunable filter, a photonic crystal fiber delivers single-mode laser light at a selected wavelength to the input of the DHT system. The laser beam is collimated using the lens L1 (Mitutoyo, 5X Plan APO NIR HR) and then split by the beam splitter BS1 into two: one passing through the sample, and thus called sample beam, and the other, called reference beam, propagating in the free space. For the condenser (CL) and objective (OL) lenses, we use the same 50X, 0.65-NA lenses (Mitutoyo, 50X Plan APO NIR HR). The reference beam is combined with the sample beam after the beam splitter BS2 and generates an interferogram at the camera plane. BS2 is slightly rotated to tilt the reference beam with respect to the sample beam and generate straight fringes[25]. Note that the optical path length changes with the wavelength, and the change occurs asymmetrically in the sample and reference beam paths, which can reduce the contrast of the interference fringes if the optical path difference is greater than the coherence length of the laser. To address this challenge, we adopted the variable optical path length (VOPL) strategy, which adjusts the optical path length of the reference beam as the wavelength is varied. For the VOPL, the mirror M1 is placed on a motorized stage (Thorlabs, MTS50-Z8) and moved to compensate for the chromatic aberration. For each wavelength, we record 100 images for varying angles of incidence onto the sample, up to 10° with respect to the optical axis. The angle of incidence is changed using a 2D large-aperture (10 mm) galvanometer scanner (Thorlabs, GVS012) installed at a plane conjugate to the sample plane. For tomographic 3D refractive index imaging, the projection images are typically recorded for a wider angular range. Although the 0.65-NA condenser lens allows us to change the incidence angle up to 40° with respect to the optical axis, the refractive index measured with SPM and microspheres increases only by 2.5×10^{-4} when we acquire 400 images using the full NA of the condenser lens. As the sample beam is rotated at the sample plane, the direction and spacing of interference fringes changes. For hyperspectral imaging, the wavelength is scanned from 1100 nm to 1650 nm with 10 nm step size. We record the raw interferograms using an InGaAs camera (Raptor Photonics, OWL 1280) with 1280 × 1024 pixels of $10\,\mu$m pixel size. The pixel resolution is $0.24\,\mu$m, and the field-of-view $307\,\mu$m × $246\,\mu$m. Without optimization for speed, it took about 8 seconds to acquire 100 interferogram images, each of 1280 × 1024 pixels, for each wavelength, and less than eight minutes to acquire the entire data set for 56 wavelengths. Although the supercontinuum laser produces the laser light covering a wide spectral range, the wavelength range available for imaging using the developed instrument is limited by the transmittance of the optical elements (e.g., the photonic crystal fiber, the objective lens) and the spectral response of the camera.

Each raw interferogram recorded with the DHT system in Fig. 1 is processed to produce the amplitude and phase images using a standard fringe analysis technique[25]. Assuming the light propagates rectilinearly across the sample, the amplitude distribution can be simply calculated using the Beer-Lambert law, and the phase distribution can be obtained with Eq. (1). Including the refraction and diffraction effect, the recorded amplitude and phase images are related to the object's absorption coefficient and refractive index in a more complex manner. According to the scalar wave theory[15], for a plane wave incident onto an object immersed in a medium, the scattered light field provides a portion of the object's spectrum in the spatial frequency space. The locus of the points (U,V,W) retrieved from the scattered light field is a hemi-spherical surface called the Ewald's sphere, where (U,V,W) represent the spatial frequency components corresponding to the spatial coordinates (X,Y,Z), respectively. The scattered light fields for varying illumination angles are similarly mapped onto the Ewald's spheres that are shifted to different directions. Noteworthy, the projection of an object along the Z direction can be related to taking the $W=0$ slice of the object's spatial frequency map, where W is the spatial frequency component corresponding to Z[26]. Thus, for SPM, we take only the $W=0$ slice of the Ewald's sphere, which is a circular ring in the U-V plane, as shown in Fig. 1(b). The scattered light fields for varying illumination angles can be mapped onto the circular rings of different radii that are shifted to different directions. After completing the mapping, the 2D inverse Fourier transform produces the synthesized phase image corresponding to the incidence angle along the optical axis direction, Z. For a more detailed description of the mapping process, the readers are referred to our previous work[12].

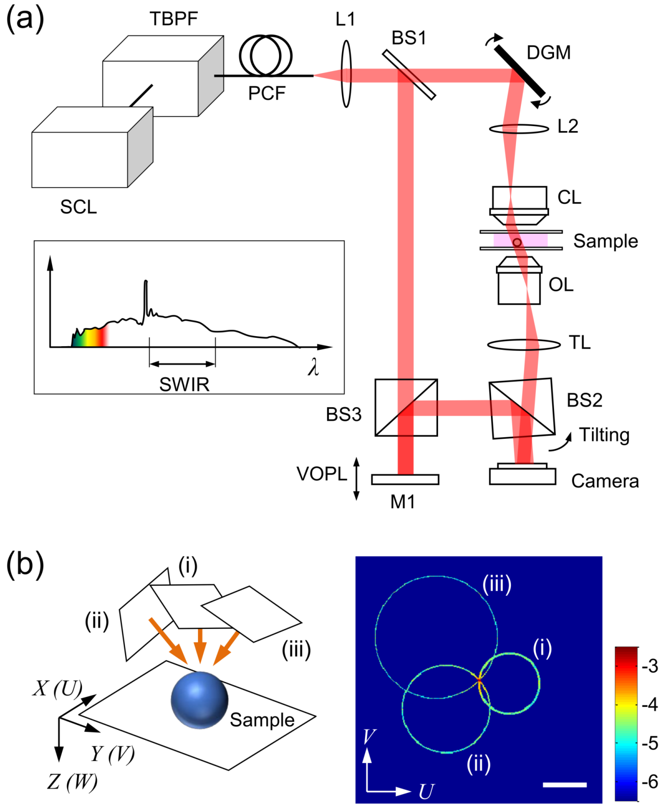

Fig. 1 Synthetic phase microscopy. (a) Schematic diagram of the short-wave infrared (SWIR) digital holographic tomography (DHT) system used in this study. SCL: supercontinuum laser; TBPF: tunable band-pass filter; PCF: photonic crystal fiber; L1 and L2: lenses; M1: mirror; BS1, BS2 and BS3: beam splitter; DGM: dual-axis galvanometer mirror; CL: condenser lens; OL: objective lens; TL: tube lens; VOPL: variable optical path length. (b) An example of mapping the scattered light fields in the U-V plane of the Fourier space (modified from the figure published by Sung et al.[12]; Copyright (2013) National Academy of Sciences). (U,V,W) represent the spatial frequency components corresponding to the spatial coordinates (X,Y,Z), respectively. The scale bar represents $1\,\mu\mathrm{m}^{-1}$, and the color bar represents the amplitude of the object's spectrum shown in the logarithmic scale of base 10.

2.2 Sample preparation and imaging procedure

Polymethyl methacrylate (PMMA) microspheres were purchased from Cospheric LLC (PMPMS-1.2 53-63 μm). Monodisperse, non-porous, silica microspheres of 20 μm diameter were purchased from Sigma (904376). Sodalime microspheres were purchased from Cospheric LLC (S-SLGMS-2.5 52-55 μm). Glycerol for molecular biology ($\geq 99.0\%$) was purchased from Sigma (G5516-500ML). FluorSave (including $\leq 0.1\%$ sodium azide as preservative) was purchased from Sigma (345789-20ML). Eukitt mounting medium was purchased from Electron Microscopy Sciences (15320). Refractive index liquids of the refractive index 1.4587, 1.40, 1.49, and 1.57, all standardized at 589.3 nm, were purchased from Cargille Laboratories. The dispersion curve for each refractive index liquid was obtained from the manufacturer.

Round coverslips of 35 mm diameter were carefully cleaned with ethanol/water (70:30, v:v) to remove any dust particles off the surface. Microspheres were spread on a coverslip, onto which 100 μL of the medium to be used with the microsphere was added. Another coverslip was gently put on the top, and the medium pushed out to the side was blotted using Kimwipe tissues. The prepared sample was put on the sample stage for about 3 hours, which provided the beads with sufficient time to settle in a non-solidifying liquid. For solidifying mounting media, 3 hours was longer than the time recommended by the manufacturers: 1 hour for FluorSave and 20 minutes for Eukitt. All measurements were done at room temperature (23 °C).

For each coverslip, a background data set was acquired, which comprises 5600 interferogram images (i.e., 100 images for 56 wavelengths) for a field of view without any samples. The background data set was used to subtract out the phase distribution not directly related to the sample, for example, the phase alteration due to the coverslip. The same background data set was used for all the samples on the same coverslip.

2.3 Data analysis

To fit the measured SPM image at each wavelength with Eq. (2), we perform a nonlinear least squares fit, which is iteratively reweighted using the bisquare weighting function. For the start point of the refractive index n_m or n_s, which is used in the fitting process, we use the value in the literature, which is often available only at a single wavelength or only in the visible wavelength range. The refractive index of ± 0.05 of the start point are given as the upper and lower bounds of the fitting. For the start point of the radius R, we use the projected area, which we obtain by thresholding the phase image. Because the projected area depends on the threshold value, the exact area of a microsphere, and thus its radius needs to be determined in the fitting. The radius values of $\pm 2\,\mu$m of the start point are given as the upper and lower bounds. For the center coordinates (x_0, y_0), the centroid coordinates of the thresholded binary image are used as the start point, then determined at a subpixel resolution within the ± 3 pixel range of the start point.

For each sample, the refractive index dispersion is measured at 10 nm step size and fit to the Cauchy-Schott equation (Sample size: 56).

$$n(\lambda) = A + B\lambda^2 + C/\lambda^2 + ..., \tag{4}$$

where A, B, C, ... are fitting coefficients. For each sample type, multiple measurements are performed and averaged to provide the mean dispersion relation. The data outside 1.5 times the standard deviation from the mean are excluded, and the remaining data are averaged to provide the mean refractive index dispersion.

3 Results and Discussions

3.1 SPM vs. conventional phase imaging

Figure 2(a) shows an example phase image recorded for one incidence angle of the illumination beam, which we refer to as conventional phase imaging. The sample is a PMMA microsphere immersed in the medium of refractive index 1.4587, and the measurement is performed for the wavelength of $1.1\,\mu$m. Although the boundary of the bead is circular, the phase distribution inside is not radially symmetric, which may be attributed to the coherent speckle noise. We also observe that the location of the peak phase value slightly shifts as the wavelength changes, which may be because the illumination beam that is slightly off axis changes the direction due to the chromatic aberration. Figure 2(b) shows the phase distribution inside the bead region as a scatter plot in the 3D space, where the height corresponds to the phase value, together with the spherical surface that is fit to the measured phase values. The outer region of the bead has a lower phase value, which would be more affected by the noise; thus, we used only the inner region for the fitting. Overall, the fitting is good with the adjusted R-squared of 0.9924. However, the root mean squared error (RMSE) is a little high as 0.1144 rad.

Figure 3(a) shows an example phase image of the same bead recorded with SPM. The phase distribution inside the bead region has much higher symmetry, and the coherent speckle has been removed. Figure 3(b) shows a scatter plot of the phase distribution inside the bead region, which is smooth. The spherical surface fit to the data overlaps well with the distribution of dots in the 3D space. The goodness of fitting has improved with the adjusted R-squared of 0.9986 and the RMSE of 0.0480 rad.

Figures 4(a) and 4(b) show the refractive index dispersion obtained with conventional phase imaging and SPM. The result ob-

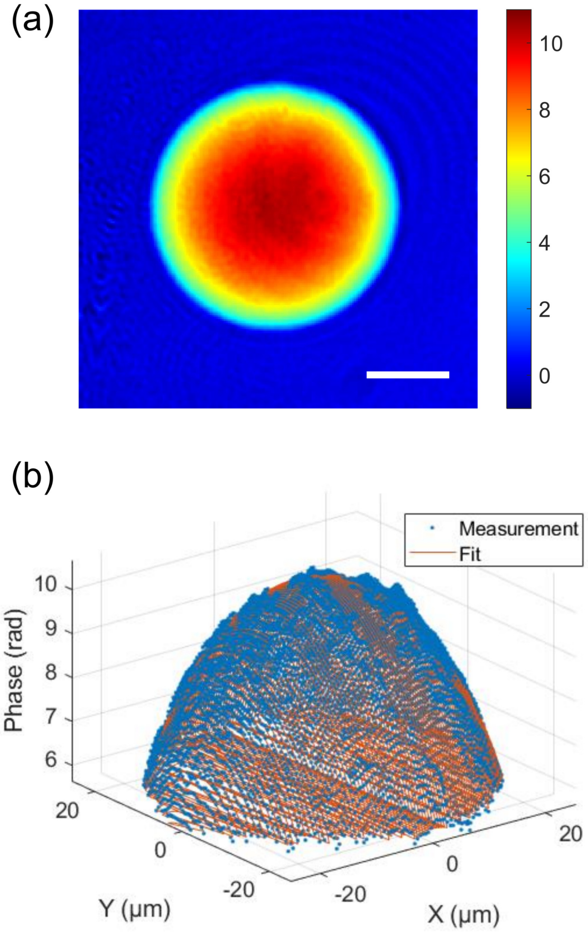

Fig. 2 Example phase image recorded for one illumination angle and a fitting of the phase distribution to Eq. (2). (a) Phase image at the wavelength of $1.1\,\mu$m for a PMMA microsphere immersed in the medium of refractive index 1.4587. (b) Phase distribution inside the bead region of (a) and a fitting using the equation for a sphere. Scale bar: $20\,\mu$m.

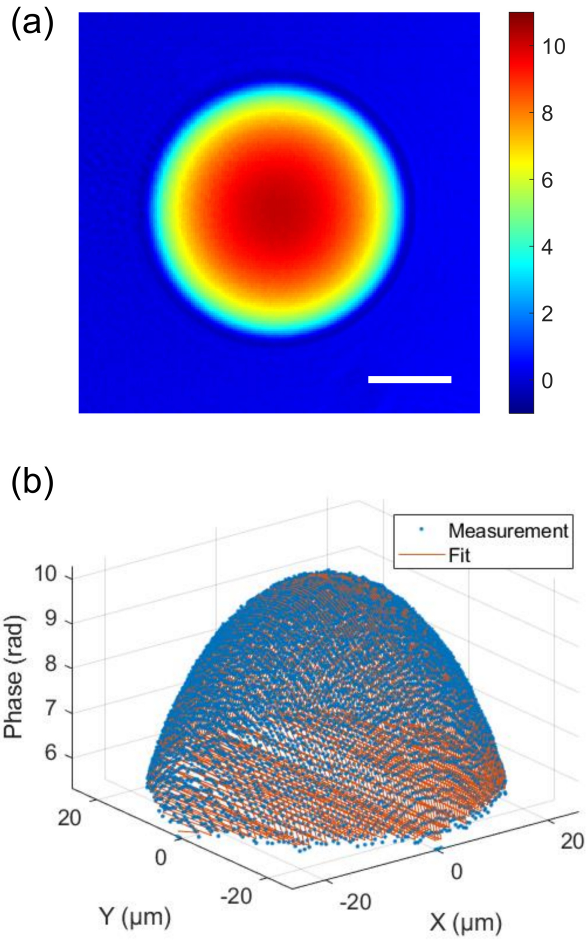

Fig. 3 Example phase image recorded with SPM and a fitting of the phase distribution to Eq. (2). (a) Synthetic phase image at the wavelength of $1.1\,\mu\text{m}$ for a PMMA microsphere immersed in the medium of refractive index 1.4587. (b) Phase distribution inside the bead region of (a) and a fitting using the equation for a sphere. Scale bar: $20\,\mu\text{m}$.

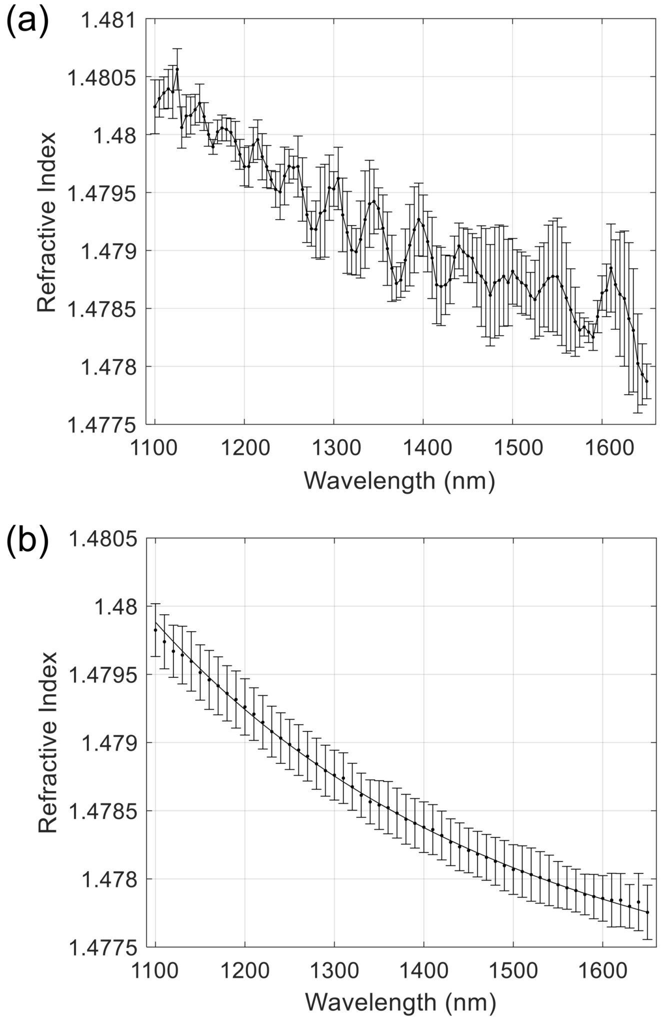

Fig. 4 Refractive index dispersion of PMMA microspheres in the 1100–1650 nm wavelength range determined with conventional phase microscopy (a) and SPM (b).

tained with five samples is averaged at each wavelength, which is shown as a solid line. The error bar represents the standard deviation of the measured values. The graph in Fig 4(a) shows an oscillation with the wavelength, which may be attributed to a slight change in the reference beam path during the wavelength scan. In a different measurement, we have confirmed that the oscillation does not relate to the physical properties of the bead. The graph in Fig 4(b) shows that the refractive index dispersion measured with SPM shows a monotonic decrease as the wavelength increases. SPM also provides a smaller standard deviation than conventional phase imaging. Although the refractive index changes only by 0.002 as the wavelength changes from 1100 nm to 1650 nm, SPM is very sensitive to detect such a small difference.

3.2 Refractive index dispersion of polymer and glass microspheres in the SWIR range

Using SPM, we have measured the refractive index dispersion of two polymer microspheres (PMMA and polystyrene) and two glass microspheres (silica and soda lime) in the SWIR range. The data fit to the Cauchy-Schott equation is summarized in Table I.

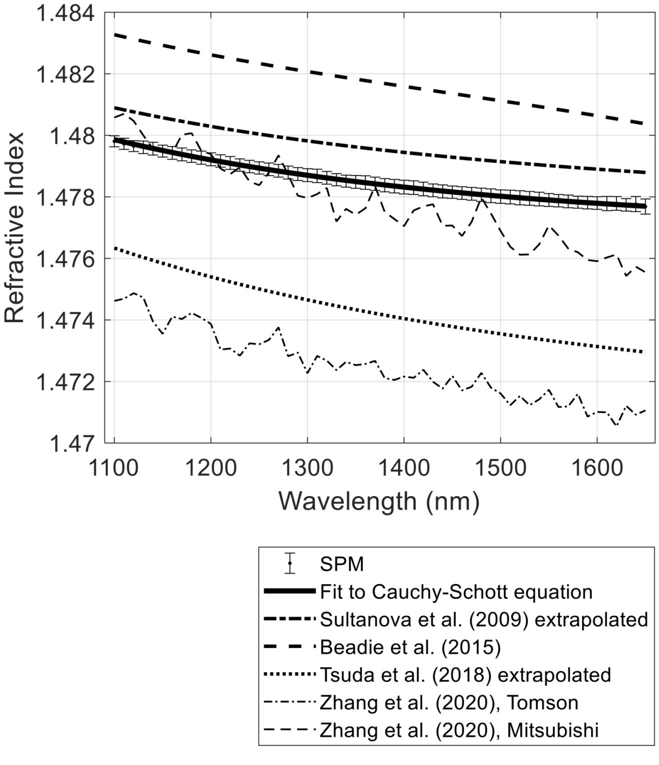

Fig. 5 Refractive index dispersion of PMMA microspheres in the 1100–1650 nm wavelength range determined with SPM and its comparison with the existing literature data.

Figure 5 shows the refractive index dispersion of PMMA microspheres measured with the refractive index liquid of 1.4587 (at 589.3 nm). The refractive index dispersion of PMMA microspheres obtained with SPM is about the average of all the literature data that were included in Fig. 5. The data can be fit to the Cauchy-Schott equation $n(\lambda) = 1.4778 - 5.7547 \times 10^{-4}\lambda^2 + 0.0023/\lambda^2$ with the RMSE of 2.6×10^{-5} (Sample size, 6). Sultanova et al. (2009)[27] used a deviation angle method to measure the refractive index dispersion of PMMA plates in the wavelength range of 0.437–1.05 μm, which is extrapolated here to the SWIR range. Using a transmission-spectrum-based method, Beadie et al. (2015)[28] measured the refractive dispersion of PMMA films in the 0.4–1.6 μm wavelength range. Using ellipsometry, Tsuda et al. (2018)[7] measured the refractive index dispersion of PMMA films in the 0.6–1 μm wavelength range, which is extrapolated here to the SWIR range. Zhang et al. (2020)[29] also used ellipsometry to measure the refractive index dispersion of PMMA films in the 0.4–2 μm wavelength range. Noteworthy, the PMMA samples from two different manufacturers (Tomson and Mitsubishi) produce different results of about 0.006. We may also attribute the difference among the reported results to different cross-linking conditions.

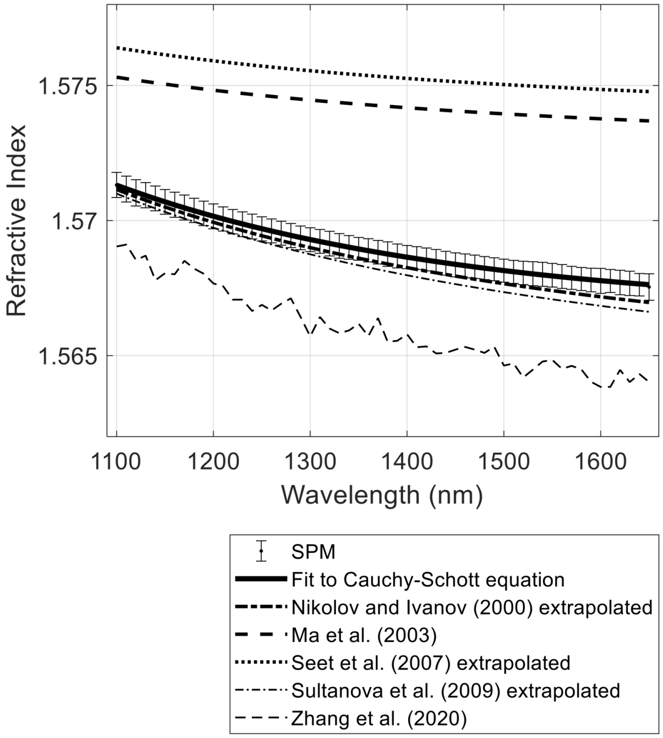

Fig. 6 Refractive index dispersion of polystyrene microspheres in the 1100–1650 nm wavelength range determined with SPM and its comparison with the existing literature data.

Figure 6 shows the refractive index dispersion of polystyrene microspheres measured with the refractive index liquid of 1.57 (at 589.3 nm). The data can be fit to the Cauchy-Schott equation $n(\lambda) = 1.5630 + 4.1159 \times 10^{-4}\lambda^2 + 0.0093/\lambda^2$ with the RMSE of 1.5×10^{-5} (Sample size, 8). The refractive index dispersion of polystyrene microspheres obtained with SPM is about the average of all the literature data shown in Fig. 6. Nikolov and Ivanov (2000)[30] measured the refractive index dispersion of injection-molded polystyrene plates using a goniometric refractometer in the 0.4–1.06 μm wavelength range. The data is extrapolated and shown in Fig. 6. Ma et al. (2003)[31] determined the refractive index dispersion of polystyrene microspheres in the 0.37–

$1.61\,\mu$m wavelength range using diffuse reflectance and transmittance measurements in combination with Monte Carlo modelling and the Mie theory. By measuring the optical extinction efficiency, Seet et al. (2007)[32] determined the refractive index dispersion of polystyrene microspheres in the 0.3–1.1 μm wavelength range, which is extrapolated here to the SWIR range. Sultanova et al.[27] used a deviation angle method to measure the refractive index dispersion of polystyrene plates in the wavelength range of 0.437–1.05 μm, which is extrapolated here to the SWIR range. Zhang et al. (2020)[29] also used ellipsometry to measure the refractive index dispersion of polystyrene films in the 0.4–2 μm wavelength range.

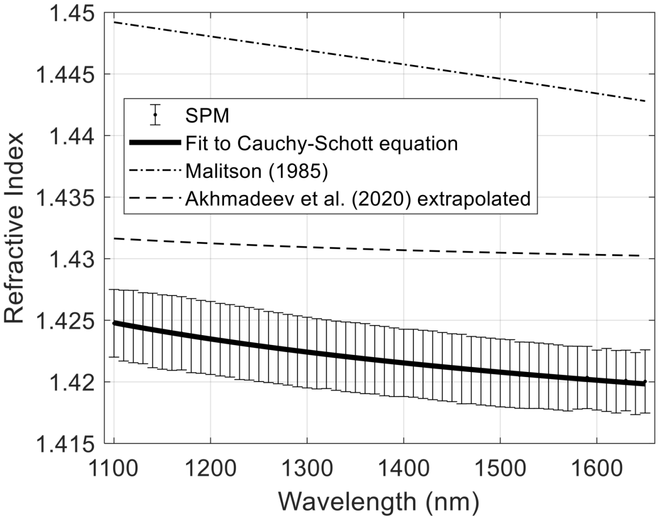

Fig. 7 Refractive index dispersion of silica microspheres in the 1100–1650 nm wavelength range determined with SPM and its comparison with the existing literature data.

Figure 7 shows the refractive index dispersion of silica microspheres measured with the refractive index liquid of 1.40 (at 589.3 nm). The result obtained with SPM can be fit to the Cauchy-Schott equation $n(\lambda) = 1.4180 - 5.4325 \times 10^{-4}\lambda^2 + 0.0090/\lambda^2$ with the RMSE of 5.8×10^{-5} (Sample size, 7). The refractive index values obtained with SPM are significantly lower than typical values for fused silica, for example, by Malitson (1985)[33]. The difference is attributed to the air nanopores that exist inside the microspheres manufactured with a Stöber method at a low temperature[34]. The large standard deviation observed with the silica microspheres is also attributed to the variation in the density of air nanopores among the microspheres. Using refractive index matching, Akhmadeev et al. (2020) measured the refractive index dispersion of the silica microspheres (diameter, 616 ± 6 nm) produced with the Stöber method. The refractive index values measured in the wavelength range of 400–1100 nm are extrapolated to the SWIR range and shown together in Fig. 7. The result obtained by Akhmadeev et al. (2020) is still higher than that obtained with SPM, which may be attributed to the different sample processing condition, measurement method, or both.

Figure 8 shows the refractive index dispersion of soda lime microspheres measured with the refractive index liquid of 1.49 (at 589.3 nm). The refractive index dispersion of the soda lime microspheres obtained with SPM can be fit to the Cauchy-Schott equation $n(\lambda) = 1.5062 - 0.0018\lambda^2 + 0.0057/\lambda^2$ with the RMSE of 1.8×10^{-5} (Sample size, 5). The values obtained for soda lime microspheres are slightly lower than those reported in Rubin (1985)[35], which may be attributed to different compositions.

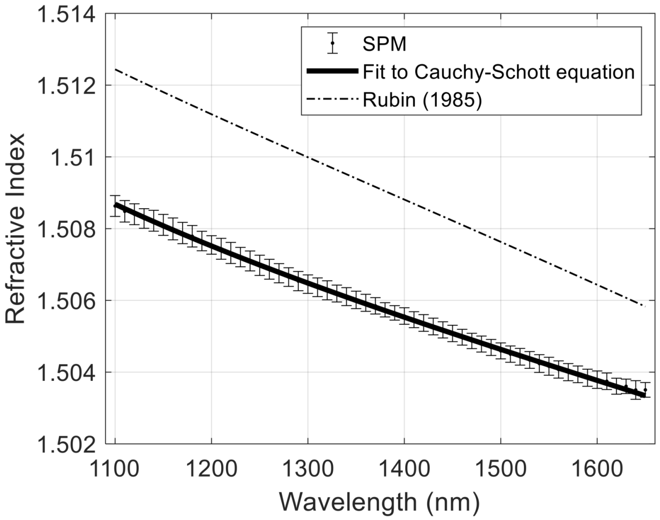

Fig. 8 Refractive index dispersion of soda lime microspheres in the 1100–1650 nm wavelength range determined with SPM and its comparison with the existing literature data.

3.3 Refractive index dispersion of microscopy mounting media in the SWIR range

The refractive index is an important parameter of microscopy mounting media because index mismatching can result in suboptimal imaging performance[36,37]. For phase imaging or refractive index imaging, the refractive index of a mounting medium is an input to the data processing and needs to be known a priori. With large penetration depth, SWIR imaging becomes popular for biomedical imaging[38–40]. The refractive index dispersion of many mounting media is not yet available in the SWIR range, to the best of our knowledge. Here we have measured the refractive index dispersion of three microscopy mounting media (glycerol, FluorSave, and Eukitt) in the 1100–1650 nm wavelength range, using the microspheres of known refractive index dispersion. For glycerol, we use PMMA microspheres. For FluorSave, we use silica microspheres, because the mounting medium may dissolve polymers, and the refractive index of silica is expected to be close to that of FluorSave. For the same reason, we use soda lime microspheres to measure the refractive index of Eukitt. The data fit to the Cauchy-Schott equation is summarized in Table II.

Figure 9 shows the refractive index dispersion of glycerol measured with PMMA microspheres. The refractive index of glycerol measured with SPM monotonically decreases from 1.4630 at 1100 nm to 1.4575 at 1650 nm. The data can be fit to the Cauchy-Schott equation $n(\lambda) = 1.4659 - 0.0033\lambda^2 + 0.0012/\lambda^2$ with the RMSE of 4.2×10^{-5} (Sample size, 5). Using Abbe refractometry, Rheims et al. measured the refractive index dispersion of glycerol

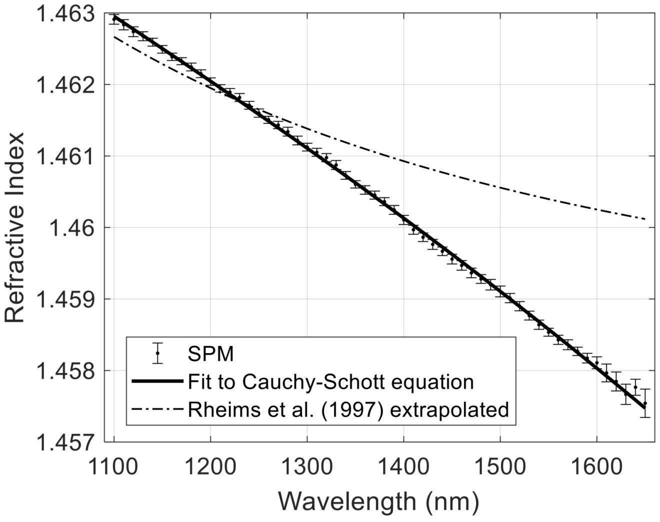

Fig. 9 Refractive index dispersion of glycerol in the 1100–1650 nm wavelength range determined with SPM and its comparison with the existing literature data.

in the 0.5893–1.05 μm wavelength range[41]. Interestingly, the refractive index dispersion of glycerol measured with SPM is slightly concave down in the measured wavelength range, while the curve extrapolated from Rheims et al. is concave up.

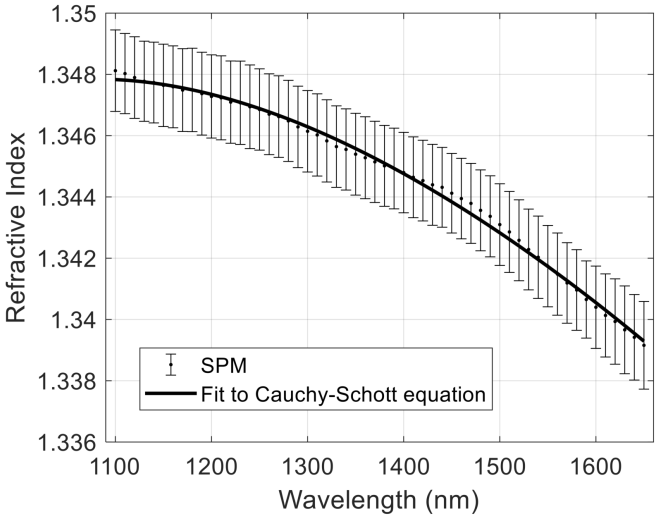

Fig. 10 Refractive index dispersion of FluorSave in the 1100–1650 nm wavelength range determined with SPM.

Figure 10 shows the refractive index dispersion of FluorSave measured with silica microspheres. FluorSave is highly recommended in immunofluorescent microscopy having strong antifade properties[42]. The refractive index of FluorSave measured with SPM monotonically decreases from 1.3478 at 1100 nm to 1.3393 at 1650 nm. The data can be fit to the Cauchy-Schott equation $n(\lambda) = 1.3703 - 0.0096\lambda^2 - 0.0131/\lambda^2$ with the RMSE of 1.7×10^{-4} (Sample size, 9).

Figure 11 shows the refractive index dispersion of Eukitt measured with soda lime microspheres. Eukitt is a very fast drying

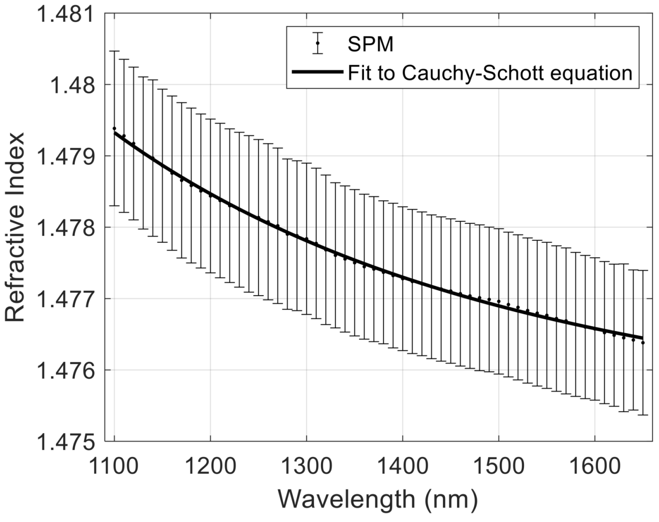

Fig. 11 Refractive index dispersion of Eukitt in the 1100–1650 nm wavelength range determined with SPM.

general-purpose resin-based mounting medium[42]. The refractive index of Eukitt monotonically decreases from 1.4793 at 1100 nm to 1.4764 at 1650 nm. The data can be fit to the Cauchy-Schott equation $n(\lambda) = 1.4736 + 1.4887 \times 10^{-4}\lambda^2 + 0.0068/\lambda^2$ with the RMSE of 3.6×10^{-5} (Sample size, 7). As shown in Fig. 11, the refractive index dispersion of Eukitt measured with soda lime microspheres has a large standard deviation (0.0010 on average). Most soda lime microspheres used for the measurement had small fragments or satellites attached to them, which may have affected the measurement. Noteworthy, we were able to determine the refractive index dispersion of soda microspheres (Fig. 8) with a small standard deviation of 2.5×10^{-4}, when excluding one outlier. According to the manufacturer, the soda lime microspheres were produced using a ”proprietary heat based process”. The reason for the large standard deviation observed in Fig. 11 remains unclear.

For microspheres, a scattering measurement and a fitting to the Mie solution is the dominant approach[8,9]. Although the Mie solution is the exact solution to the Maxwell’s equations, and thus is accurate, the scattering analysis is affected by the signal-to-noise ratio of the scattering measurement, which may vary with the size and refractive index of the microsphere as well as the measurement geometry. Here we used SPM to measure the scattering-corrected phase distribution, which was then fit to a theoretical model assuming the rectilinear propagation of light across the microsphere. The phase measurement is more sensitive than the measurement of the scattered intensity. Using SPM, the effect of scattering at the sample’s boundary can be corrected, and the coherent speckle noise and the oblique incidence of illumination, which can affect the accuracy of conventional phase imaging, can be minimized. We note that SPM, as with conventional phase imaging, requires phase unwrapping, which may affect the accuracy of the phase measurement and eventually fail if the refractive index of the microsphere is very different from that of the surrounding medium. A rigorous comparison of SPM with the

Mie scattering analysis is left for our future work.

Table 1 Summary of the refractive index dispersion (1100–1650 nm) of the microspheres determined in this study. λ is the wavelength in μm.

Material	Dispersion equation	RMSE
PMMA	$n(\lambda) = 1.4778 - 5.7547 \times 10^{-4}\lambda^2 + 0.0023/\lambda^2$	2.6×10^{-5}
PS	$n(\lambda) = 1.5630 + 4.1159 \times 10^{-4}\lambda^2 + 0.0093/\lambda^2$	1.5×10^{-5}
Silica	$n(\lambda) = 1.4180 - 5.4325 \times 10^{-4}\lambda^2 + 0.0090/\lambda^2$	5.8×10^{-5}
Soda lime	$n(\lambda) = 1.5062 - 0.0018\lambda^2 + 0.0057/\lambda^2$	1.8×10^{-5}

Table 2 Summary of the refractive index dispersion (1100–1650 nm) of the microscopy mounting media determined in this study. λ is the wavelength in μm.

Material	Dispersion equation	RMSE
Glycerol	$n(\lambda) = 1.4659 - 0.0033\lambda^2 + 0.0012/\lambda^2$	4.2×10^{-5}
FluorSave	$n(\lambda) = 1.3703 - 0.0096\lambda^2 - 0.0131/\lambda^2$	1.7×10^{-4}
Eukitt	$n(\lambda) = 1.4736 + 1.4887 \times 10^{-4}\lambda^2 + 0.0068/\lambda^2$	3.6×10^{-5}

4 Summary

In this work, we demonstrated SPM to measure the refractive index of homogeneous microspheres and liquids. Using SPM, we determined the refractive index dispersion of two polymer microspheres (PMMA and polystyrene), two glass microspheres (silica and soda lime), and three microscopy mounting media (glycerol, FluorSave, and Eukitt) in the SWIR range of 1100–1650 nm. Further explorations can be made in the future to obtain the refractive index of different materials in other wavelength ranges.

Author Contributions

Y.S. developed the concept; M.N, C.J., P.S. and Y.S. performed the experiments and analyzed the data; all authors wrote the manuscript.

Conflicts of interest

There are no conflicts to declare.

Acknowledgments

This research was funded by the National Science Foundation (1808331).

References

1 E. Thimsen, B. Sadtler and M. Y. Berezin, *Nanophotonics*, 2017, **6**, 1043–1054.

2 S. Serranti, L. Fiore, G. Bonifazi, A. Takeshima, H. Takeuchi and S. Kashiwada, *Proc. SPIE*, 2019, **11197**, 1119710.

3 R. Xu, *Particuology*, 2015, **18**, 11–21.

4 G. Popescu, *Quantitative Phase Imaging of Cells and Tissues*, McGraw-Hill Education, New York, NY, 2011.

5 P. González-Rodríguez and A. D. Kim, *Opt. Express*, 2009, **17**, 8756–8774.

6 S. Kedenburg, M. Vieweg, T. Gissibl and H. Giessen, *Opt. Mater. Express*, 2012, **2**, 1588–1611.

7 S. Tsuda, S. Yamaguchi, Y. Kanamori and H. Yugami, *Opt. Express*, 2018, **26**, 6899–6915.

8 M. R. McGrory, M. D. King and A. D. Ward, *J. Phys. Chem. A*, 2020, **124**, 9617–9625.

9 P. Müller, M. Schürmann, S. Girardo, G. Cojoc and J. Guck, *Opt. Express*, 2018, **26**, 10729–10743.

10 M. Rinehart, Y. Zhu and A. Wax, *Biomed. Opt. Express*, 2012, **3**, 958–965.

11 J.-H. Jung, J. Jang and Y. Park, *Anal. Chem.*, 2013, **85**, 10519–10525.

12 Y. Sung, A. Tzur, S. Oh, W. Choi, V. Li, R. R. Dasari, Z. Yaqoob and M. W. Kirschner, *Proc. Natl. Acad. Sci. U.S.A.*, 2013, **110**, 16687–16692.

13 S. A. Alexandrov, T. R. Hillman, T. Gutzler and D. D. Sampson, *Phys. Rev. Lett.*, 2006, **97**, 168102.

14 M. Kim, Y. Choi, C. Fang-Yen, Y. Sung, R. R. Dasari, M. S. Feld and W. Choi, *Opt. Lett.*, 2011, **36**, 148–150.

15 M. Born and E. Wolf, *Principles of Optics: Electromagnetic Theory of Propagation, Interference and Diffraction of Light*, Elsevier, 2013.

16 W. Choi, C. Fang-Yen, K. Badizadegan, S. Oh, N. Lue, R. R. Dasari and M. S. Feld, *Nat. Methods*, 2007, **4**, 717–719.

17 O. Haeberlé, K. Belkebir, H. Giovaninni and A. Sentenac, *J. Mod. Opt.*, 2010, **57**, 686–699.

18 Y. Sung, W. Choi, C. Fang-Yen, K. Badizadegan, R. R. Dasari and M. S. Feld, *Opt. Express*, 2009, **17**, 266–277.

19 J. Jung, K. Kim, J. Yoon and Y. Park, *Opt. Express*, 2016, **24**, 2006–2012.

20 Y. Sung, *Phys. Rev. Appl.*, 2018, **10**, 054041.

21 Y. Sung, *Phys. Rev. Appl.*, 2023, **19**, 014064.

22 Y. Sung and R. R. Dasari, *J. Opt. Soc. Am. A*, 2011, **28**, 1554–1561.

23 J. Lim, K. Lee, K. H. Jin, S. Shin, S. Lee, Y. Park and J. C. Ye, *Opt. Express*, 2015, **23**, 16933–16948.

24 M. Bertero, P. Boccacci and C. De Mol, *Introduction to Inverse Problems in Imaging*, CRC press, 2021.

25 K. Creath, *Prog. Optics*, 1988, **26**, 349–393.

26 A. C. Kak and M. Slaney, *Principles of Computerized Tomographic Imaging*, IEEE press New York, 1988.

27 N. Sultanova, S. Kasarova and I. Nikolov, *Acta Phys. Pol. A*, 2009, **116**, 585–587.

28 G. Beadie, M. Brindza, R. A. Flynn, A. Rosenberg and J. S. Shirk, *Appl. Opt.*, 2015, **54**, F139–F143.

29 X. Zhang, J. Qiu, X. Li, J. Zhao and L. Liu, *Appl. Opt.*, 2020, **59**, 2337–2344.

30 I. D. Nikolov and C. D. Ivanov, *Appl. Opt.*, 2000, **39**, 2067–2070.

31 X. Ma, J. Q. Lu, R. S. Brock, K. M. Jacobs, P. Yang and X.-H. Hu, *Phys. Med. Biol.*, 2003, **48**, 4165.

32 K. Y. Seet, R. Vogel, T. A. Nieminen, G. Knöner, H. Rubinsztein-Dunlop, M. Trau and A. V. Zvyagin, *Appl. Opt.*, 2007, **46**, 1554–1561.

33 I. Malitson, *J. Opt. Soc. Am.*, 1985, **55**, 1205–1209.

34 F. Garcia-Santamaria, H. Miguez, M. Ibisate, F. Meseguer and C. Lopez, *Langmuir*, 2002, **18**, 1942–1944.

35 M. Rubin, *Sol. Energy Mater.*, 1985, **12**, 275–288.

36 A. Diaspro, F. Federici and M. Robello, *Appl. Opt.*, 2002, **41**, 685–690.

37 R. McGorty, J. Schnitzbauer, W. Zhang and B. Huang, *Opt. Lett.*, 2014, **39**, 275–278.

38 E. Thimsen, B. Sadtler and M. Y. Berezin, *Nanophotonics*, 2017, **6**, 1043–1054.

39 J. Cao, B. Zhu, K. Zheng, S. He, L. Meng, J. Song and H. Yang, *Front. Bioeng. Biotechnol.*, 2020, **7**, 487.

40 C. Juntunen, A. R. Abramczyk, P. Shea and Y. Sung, *Sensors*, 2023, **23**, 5164.

41 J. Rheims, J. Köser and T. Wriedt, *Meas. Sci. Technol.*, 1997, **8**, 601.

42 F. Saify and N. Tiwari, *OMPJ*, 2020, **11**, 20–24.